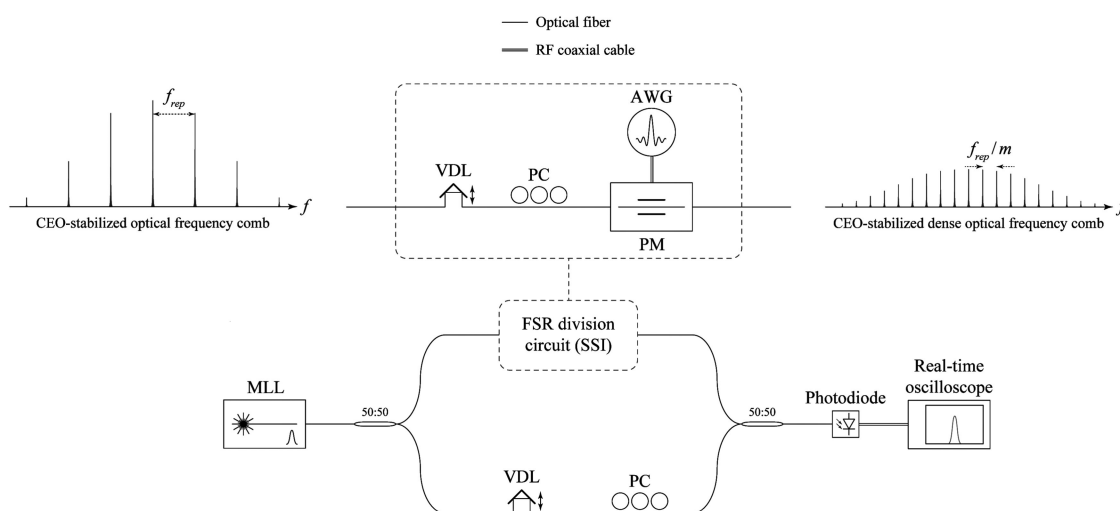# Ultra-Dense CEO-Stabilized Broadband Optical Frequency Comb Generation Through Simple, Programmable, and Lossless 1000-Fold Frequency-Spacing Division

Xiao-Zhou Li
Mohamed Seghilani
Reza Maram
Luis Romero Cortés
José Azaña

Ultra-Dense CEO-Stabilized Broadband Optical Frequency Comb Generation Through Simple, Programmable, and Lossless 1000-Fold Frequency-Spacing Division

Xiao-Zhou Li [1,2] **Mohamed Seghilani,** [1] **Reza Maram,** [1] **Luis Romero Cortés,** [1] **and José Azaña** [1]

[1] Institut National de la Recherche Scientifique – Énergie, Matériaux et Télécommunications (INRS-EMT), 800 de la Gauchetière Ouest, Montréal, QC H5A1K6, Canada
[2] School of Optoelectronic Engineering and Instrumentation Science, Dalian University of Technology, Dalian 116024, China

Abstract: Ultra-dense broadband optical frequency combs with sub-MHz frequency spacing and stabilized carrier-envelope offset (CEO) are needed for many important applications, including high-accuracy real-time sub-Doppler spectroscopy, precise characterization of photonic devices, and greenhouse gas sounding. However, the generation of such combs remains very challenging because they require mode-locked lasers with impractically long cavities ($>$few hundred meters). Here we demonstrate a CEO-stabilized optical frequency comb with a programmable sub-MHz frequency spacing, obtained through simple, suitable temporal phase modulation of a 250-MHz input comb. The method preserves the energy, the bandwidth, and the CEO-stabilization of the input comb, achieving a combined (CEO and repetition-rate) integrated phase noise below $\pi/10$, and a frequency spacing down to 250 kHz over a 5-dB bandwidth of 10 THz, i.e., corresponding to a record high 1000-fold frequency spacing reduction and more than 40 000 000 comb lines. The demonstrated method bridges the gap between presently available high-quality optical frequency combs and a host of demanding and important applications that require CEO-stabilized broadband frequency combs with sub-MHz spacings.

Index Terms: Noise characterization, Optical frequency comb, Talbot and self-imaging effects.

1. Introduction

Optical frequency combs (OFCs) have revolutionized the fields of optical metrology and optical sensing [1]. The stabilization of the carrier-envelope offset (CEO) in OFCs achieved over two decades ago made it possible to know the exact frequency of a given comb tooth with a microwave-level accuracy [2]. This opened the path to many advanced applications, such as frequency metrology [3]–[5], high-resolution time-resolved spectroscopy [6]–[8], and the control of atomic-scale electron

dynamics [9], [10]. OFCs are mainly generated using mode-locked lasers (MLLs), which can routinely provide broadband OFCs with frequency spacings – the free spectral range (FSR) – ranging from a few tens of MHz to a few tens of GHz [11], [12]. However, the generation of CEO-stabilized broadband OFCs with sub-MHz FSRs remains a significant challenge as this requires the use of impractically long laser cavities (e.g., $\sim$150 m for an FSR = 1 MHz).

This limitation prevents current OFCs from reaching their full potential in several important applications, in particular those related to ultra-high-resolution spectroscopy. In these applications, each line of the comb is utilized as an individual spectral sampling point, and as a result, all the spectral features within a broad frequency spectrum can be recorded simultaneously allowing for simple and fast measurement [13], [14]. When the comb's CEO is stabilized, frequency resolutions of a few kHz can be reached, exceeding the accuracy of conventional spectroscopy methods by many orders of magnitude [15]. However, for fast (eventually, single-shot) measurements, the frequency resolution is directly dictated by the comb's FSR. Hence, available broadband CEO-stabilized combs have FSRs that are far too large to interrogate spectral features narrower than a few MHz, such as those found in electromagnetically-induced resonances [16], and hyperfine transitions [17], [18]. An accurate characterization of these features would require many comb lines to fit within each feature, thus calling for comb FSRs in the sub-MHz range or below. Therefore, the availability of CEO-stabilized ultra-dense OFCs would open the path to many important applications that require fast and simultaneous interrogation of broad spectra ($>$1 THz) with sub-MHz resolution and ultra-high frequency accuracy. Examples of such applications include: the precise characterization of a wide range of photonic devices [19], [20], greenhouse gas sounding [21], [22], detection of terrestrial-mass planets around M-dwarfs [23], low pressure molecular gas spectroscopy [24], [25], and even the redefinition of the second [26], [27].

To address the lack of ultra-dense OFCs, different solutions have been proposed, most prominently electro-optic OFC generation [7], [16], [17], FSR reduction using pulse-picking [24], and pseudo-random binary phase modulation [28]. Most of these methods allow for FSR reduction, down to the sub-MHz regime [7], [16], [17], [28]. However, pulse picking is inherently very lossy, as it implies the deliberate discarding of a large portion of the original comb energy. Narrow-spacing OFCs generated by direct electro-optic methods exhibit very limited bandwidths, typically lower than a few tens of GHz [7], [17], [29], orders of magnitude below that of conventional MLL-generated OFCs. Besides, approaches based on pseudo-random binary phase modulation are limited by the choice of FSR division factors and the random phases may not be known a priori. Most importantly, to our knowledge, previous works on OFC generation with sub-MHz FSRs, rarely address the critical issue of CEO stability, despite its crucial importance for many practical applications.

In this work, we use Spectral Talbot Self-Imaging (SSI) [30], [31] to generate a programmable, ultra-dense (250-kHz), and CEO-stabilized optical frequency comb through FSR division (by up to 3 orders of magnitude) of a commercial 250-MHz CEO-stabilized comb. The demonstrated method is induced by a simple, suitably designed temporal phase modulation of the original OFC, inherently preserving the comb's initial frequency bandwidth and energy. The latter is merely redistributed into the target ultra-dense comb, except for practical insertion losses of the modulator. Moreover, the method allows for an independent electronic tuning of the FSR division factor. We experimentally demonstrate odd and even division factors, ranging from 2 to a record high of 1000. Since SSI rearranges the structure of the input frequency comb, a key question remains to be sorted out: what effect does this rearrangement have on the CEO-frequency and its stabilization? For the first time, we demonstrate here that SSI keeps the CEO frequency unaltered and preserves very nearly the phase noise characteristics of the input comb. This is evidenced by experimental measurements that show a very low added phase noise, below $\pi/10$ (integrated value), which corresponds to a phase fluctuation of less than 5% root mean square (RMS). Based on this finding, this work shows a simple, yet very powerful, method to generate broadband ultra-dense CEO-stabilized OFCs with programmable FSR, down to the kHz range, beyond the performance capabilities of current mode-locked lasers.
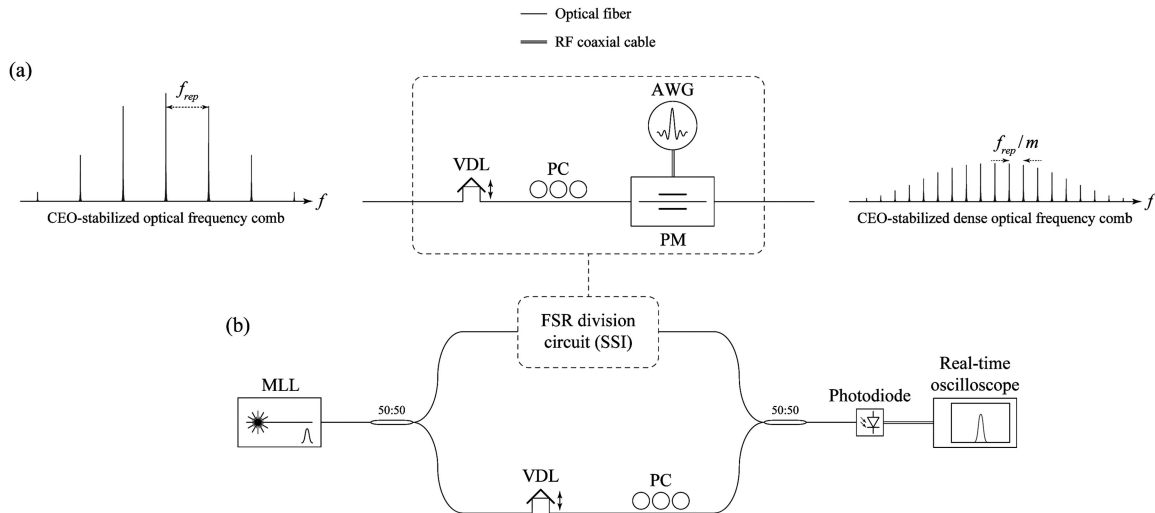
Fig. 1. (a) Experimental setup for FSR reduction of a CEO-stabilized optical frequency comb by spectral self-imaging. The input FSR is reduced by an integer factor m by modulating the corresponding pulse train with an appropriate temporal Talbot phase profile (see Eq. (1)). (b) Optical heterodyne setup for high resolution optical frequency comb characterization. MLL: Mode-locked laser; AWG: Arbitrary waveform generator; VDL: Variable delay line; PC: Polarization controller; PM: Phase modulator.

2. Materials and Methods

The circuit schematic of the experimental setup for ultra-dense CEO-stabilized comb generation is illustrated in Fig. 1. Based on a commercial CEO-stabilized OFC, the comb FSR is divided using a programmable temporal phase modulation scheme, shown in Fig. 1(a), while the output OFC and its CEO stability is characterized using optical heterodyne detection, as depicted in Fig. 1(b).

2.1 FSR Division by Spectral Self-Imaging

SSI is induced on a phase-coherent OFC through modulation of the corresponding temporal pulse train with a periodic phase sequence defined by the theory of the Talbot effect, as follows [32]–[37]:

$$\phi_n = \pi \frac{s}{m} n^2 \ (\mathrm{mod}\ 2\pi),\tag{1}$$

where ϕ_n is the phase level to be applied to the nth pulse of the incoming periodic temporal pulse train, and s and m are two mutually-prime natural numbers. This results in an OFC with the same overall energy and identical features (self-imaged spectral envelope and bandwidth) to those of the input one, but with an FSR that is divided by the integer number m. In this design, s is a free parameter to be fixed at the designer's convenience.

Our experimental setup for SSI-driven FSR division is shown in Fig. 1(a). The input OFC is generated using a commercial mode-locked fiber laser (Menlo-UL250), with an FSR $f_{rep}^{(1)} = 250$ MHz over a spectral bandwidth of ~ 10 THz (measured at 5 dB from the maximum spectral intensity). This MLL has a stabilized CEO frequency, f_{CEO}, achieved through the standard $f - 2f$ CEO-stabilization approach [2], [38]. The evolution of f_{CEO} in time and its Allan deviation are shown in Fig. 6 of the Appendix (Section 6.1) at the end of this paper. The SSI stage consists of a temporal phase modulator (EOSpace, 10 GHz bandwidth) preceded by a variable delay line and a polarization controller, used to align the modulation function to the optical signal and to maximize the modulation efficiency. The modulator is driven by an arbitrary waveform generator (AWG, Tektronix AWG7122C, 7.5 GHz bandwidth), which allows us to program the appropriate Talbot phase sequence, according to Eq. (1). The above FSR division process enables the generation of a new comb as shown in Fig. 1(a), where the output frequency spacing is $f_{rep}^{(2)} = f_{rep}^{(1)} / m$.

2.2 Optical Heterodyne Detection for Comb Characterization

For a more thorough characterization of the generated OFC, we used a conventional heterodyne detection scheme. For this, the generated FSR-divided OFC was mixed with the original comb [39], [40] and the resulting photodetected beat signal was recorded with a real-time oscilloscope (see Fig. 1(b)). This comb heterodyne scheme is equivalent to a dual comb spectroscopy detection setup in the particular case where the FSR of one of the mixing OFC signals is an integer multiple of the other OFC [5], [36], [37]. To implement the heterodyning process, we used a 50:50 fiber coupler to divide the laser output into two identical branches. The comb in the first branch undergoes FSR division through the SSI process. In the second branch, the comb is kept unchanged; only adding a tunable delay line and a polarization controller to optimize the power of the beatnote, i.e., to ensure that the individual pulses in the two branches are synchronized and have the same polarization (note that if a polarization maintaining fiber is used, the polarization controller is not needed). Next, the two branches are mixed using another fiber-based directional coupler as a combiner, followed by a 50-GHz photodetector (Finisar XPDV) that converts the optical beat into an RF signal.

The RF spectrum of the recorded beat signal provides precise information on several features of the generated FSR-divided comb, most importantly (i) its output frequency spacing $f_{rep}^{(2)} = f_{rep}^{(1)}/m$, (ii) any detuning of the CEO frequency with respect to the input one δf_{CEO}, and (iii) potential excess phase noise of the CEO and the repetition rate added by the FSR division process, Δf_{CEO}^{excess} and Δf_{rep}^{excess}, respectively. To demonstrate this, we write down the expression of the beatnote spectrum as follows:

$$\nu_N^{(2)} - \nu_M^{(1)} = f_{rep}^{(1)}(N/m - M) + \delta f_{CEO} + \Delta f_{rep}^{excess}(t) + \Delta f_{CEO}^{excess}(t) \tag{2}$$

This equation represents the RF spectrum in the general case of a beating between two optical frequencies: the Mth line of Comb 1 and the Nth line of Comb 2, $\nu_M^{(1)}$ and $\nu_N^{(2)}$ respectively. Note that in deriving Eq. (2), we have considered that the Comb 2 is generated by dividing the FSR of Comb 1 m-fold, i.e., $f_{rep}^{(2)} = f_{rep}^{(1)}/m$. The detailed analytical calculations to obtain Eq. (2) are summarized in the Appendix (Section 6.2) at the end of this paper.

Equation 2 implies that the beat signal spectrum is composed by a periodic set of spectral lines spaced by the divided FSR $f_{rep}^{(1)}/m$. In particular, all the lines $\nu_N^{(2)}$ and $\nu_M^{(1)}$ from Comb 2 (output) and Comb 1 (input) satisfying the condition $N = k + mM$ contribute to the power of the kth harmonic of the resulting beat signal at the divided FSR frequency. The equation also shows that any shift in the CEO frequency of the input comb, δf_{CEO}, induced by the FSR division process will be visible in the beat signal spectrum because this would correspondingly detune the frequency of each of the resulting beatnotes. Most importantly, the spectrum of the phase noise (of the FSR and CEO) added by the FSR division method can be directly inferred from the analysis of anyone of these beatnotes. In particular, those close to DC (the 1st or 2nd harmonics) can be easily analyzed using relatively low speed detectors and digital signal processing, as shown in the next section.

2.3 Phase Noise Spectrum Calculation Using Digital Beatnote Demodulation

The beatnotes generated by the optical heterodyne setup (Fig. 1(b)) contain all the information about the variation of the laser field in time, including its phase. The digital beatnote demodulation method provides a direct access to this instantaneous phase profile without the need for a complex frequency discrimination setup, which also typically requires shielding from the environmental noise and a precise calibration. Briefly, to obtain the phase profile of the laser field, the beatnote's electrical signal $b(t)$ generated by the photodetector is first acquired, in a single shot, by the digital sampler of the real-time oscilloscope (Agilent DSO-X 92804A, with an analog bandwidth of 28-GHz and a maximum sampling rate of 80 Gs/s). Next, we apply the Hilbert transform $\mathcal{H}[\cdot]$ to the beatnote signal to construct the so-called analytic signal $b_a(t)$ associated with the recorded real-valued signal, $b(t)$ [41]:

$$b_a(t) = b(t) + i\mathcal{H}[b(t)], \tag{3}$$

where i is the imaginary unit. The instantaneous phase is then extracted using the well-known properties of complex numbers as follows: $\varphi(t) = arctan(\mathcal{H}[b(t)]/b(t))$. This phase can be written

as the sum of an average phase φ_0 and a fluctuating phase $\tilde{\varphi}(t)$. Finally, the power spectral density (PSD) of the phase noise PSD_φ is obtained by calculating the Fourier transform of the auto-correlation of the fluctuating phase [41].

3. Experimental Results

The experimental results of ultra-dense OFC generation and CEO-stability characterization are reported in this section. Different FSR division factors are implemented, and their corresponding optical spectra (from direct detection in Fig. 1(a)) and RF spectra (from heterodyne detection in Fig. 1(b)) are presented. The key features of CEO stabilization, spectral shape and bandwidth are then investigated by comparing the input and output combs, which elucidate the feasibility of our approach for sub-MHz comb generation without altering the CEO-stabilization and bandwidth of the original frequency comb.

3.1 Sub-MHz FSR

Experimentally, we derived the phase sequences ϕ_n from Eq. (1) for different FSR division factors, in particular $m = 2, 5, 10, 50, 250, 500,$ and 1000. The parameter s can be arbitrarily chosen as long as it is co-prime to m, which enables the possibility of using various different forms of the modulation phase sequences. In this work, we use $s = 1$ for simplicity, but it should be noted that other choices of s will also lead to similar successful FSR division operations. Fig. 2(a) shows the modulation phase sequence ϕ_n generated by the AWG for the cases with $m = 2, 5, 250,$ and 1000. The resulting output signals after temporal phase modulation are shown in Figs. 2(b) and 2(c). In Fig. 2(b), the measured optical spectra of the first 3 generated OFCs exhibit the predicted decrease of the frequency spacings by factors of 2, 5, and 10, respectively, with respect to the input optical spectra obtained when the temporal phase modulation is not applied (PM OFF). Since this technique involves phase-only temporal modulation, conservation of energy ensures that the total signal power remains unchanged. Thus, the power of each output comb line is reduced accordingly as compared to that of the input. The spectra shown in Fig. 2(b) were measured using a high resolution (5 MHz) optical spectrum analyzer (OSA) (Apex, AP2440A). While this measurement is straightforward, OFCs generated by higher division factors (i.e., for $m > 10$) cannot be resolved through this method. To overcome this, we used the optical heterodyne method described in Sections 2.2 and 2.3.

Fig. 2(c) shows the RF spectrum measured at the output of the photodiode in Fig. 1(b) for different FSR division factors of 2, 5, 250, and 1000. It is found that the measured beatnotes match exactly $f_{rep}^{(1)}/m$ (the input FSR reduced m − fold) without any observable detuning, which indicates that the CEO frequency remains unchanged (within a 50-Hz uncertainty of the measurement, limited by the oscilloscope memory), regardless of the FSR division factor, m. In sum, the experimental beatnote RF spectra (Fig. 2(c)) show successful generation of ultra-dense OFCs with an FSR as low as 250 kHz starting from 250 MHz, achieving a record high FSR reduction of 3 orders of magnitude, while keeping the CEO frequency unchanged.

On the other hand, the fluctuations of the output comb CEO add up to the FSR's fluctuations to form the comb's phase noise in excess with respect to the input comb. To characterize this noise, we calculated its PSD using the digital beatnote demodulation method described above (Section 2.3), results discussed in the following section.

3.2 CEO-Stabilization

Fig. 3(a) shows the obtained phase noise PSD for $m = 2$ and $m = 1000$, as compared with the reference level measured without phase modulation (PM OFF). These measurements demonstrate that there is nearly no added noise for small division factors, as is shown by the PSD curves for $m = 2$ and PM OFF. The phase noise generally increases as the division factor m is further increased (not shown here). For $m = 1000$, the excess phase noise is typically 15 dB higher than the reference level, with an integrated value (right-axis) that keeps under $\pi/10$ (i.e., $<5\%$ root mean square (RMS) fluctuations) over the whole measurement bandwidth. It should be noted that the
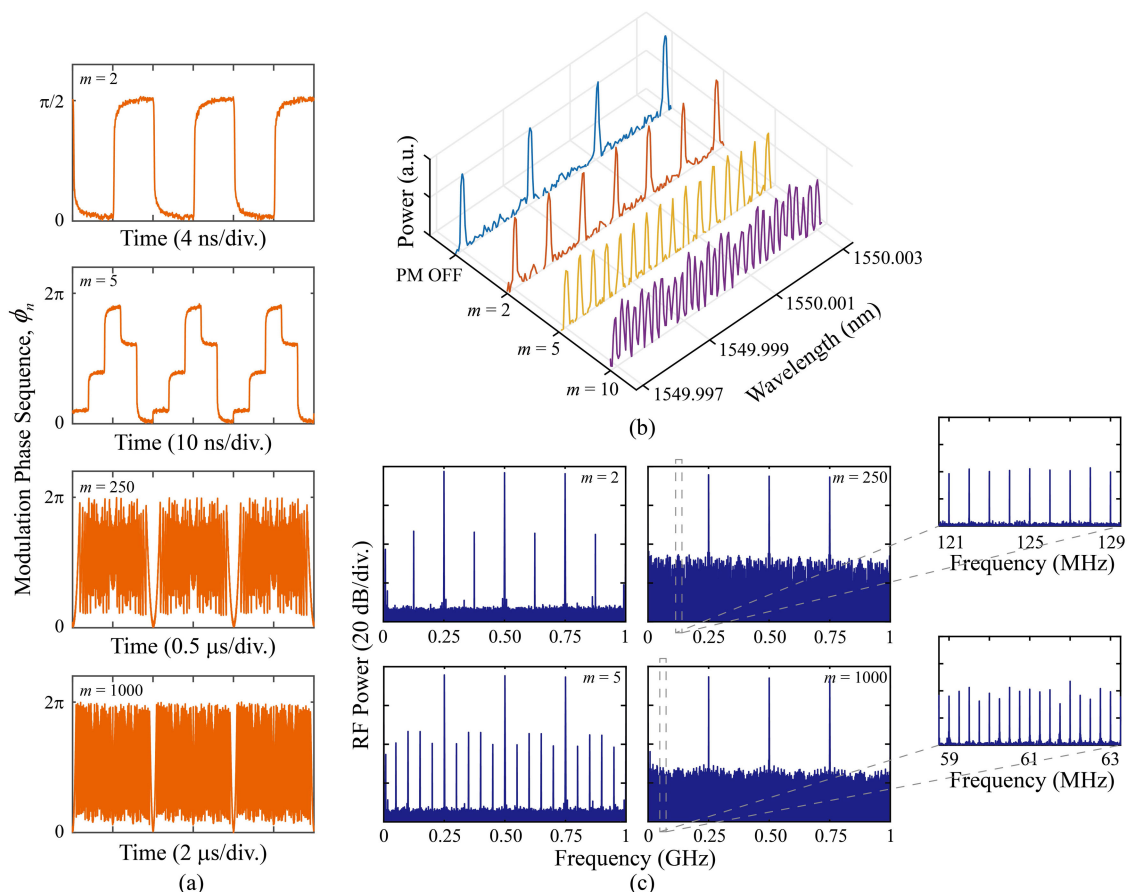
Fig. 2. (a) Modulation phase sequence obtained by setting $m = 2, 5, 250, 1000$ in Eq. (1). (b) Measured optical spectra of output OFCs obtained with $m = 2, 5, 10$. The input OFC's spectrum (PM OFF) is shown for reference. (c) High-resolution RF spectra obtained with the optical heterodyne setup for $m = 2, 5, 250, 1000$ (measured with a sampling rate of 40 GHz). The zoomed-in spectra corresponding to the cases $m = 250, 1000$ are also shown (measured with a sampling rate of 1 GHz).
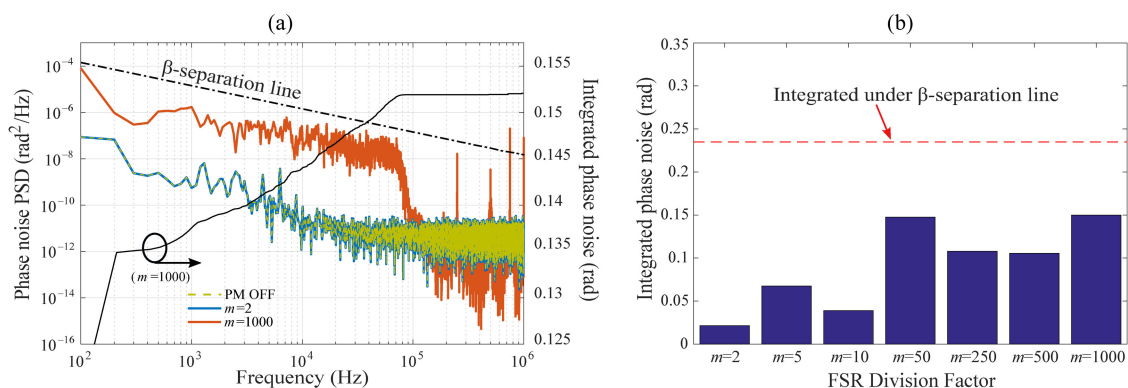

Fig. 3. (a) Left axis: PSD of the output OFC excess phase noise obtained for the FSR division factors of $m = 2$ and $m = 1000$. The β-separation line is shown for reference. Right axis: integrated phase noise in the output comb for $m = 1000$. (b) Integrated phase noise, over the bandwidth [50 Hz–250 MHz], for different FSR division factors. The phase noise integrated under the β-separation line is shown for reference.
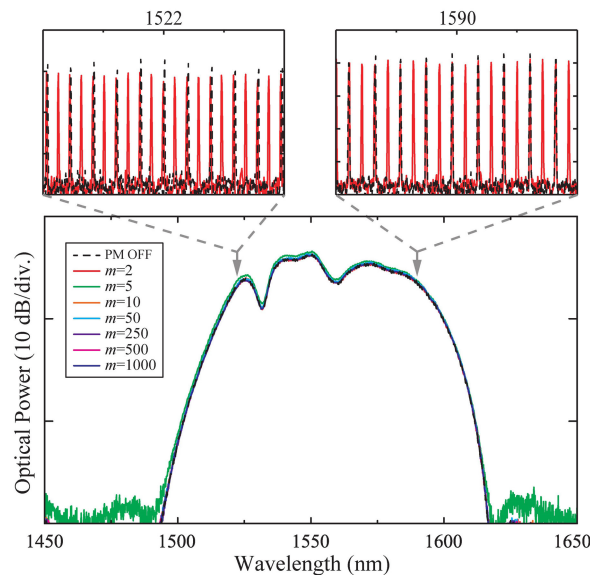
Fig. 4. Full width spectra of some of the generated ultra-dense OFCs (with the FSR division factor m increasing from 2 to 1000). The initial OFC spectrum (PM OFF) is shown for reference. The two inset figures zoom into two regions spaced at 80 THz (~70 nm) in the spectrum obtained with $m = 2$. Note that because of the limited resolution of the OSA (20 MHz), the levels of all the measured spectra look identical. This is due to the fact that for each measurement point, the OSA integrates the power of all adjacent unresolved frequency points.

measured excess phase noise always keeps below the β-separation line [42] (dashed dotted line in Fig. 3(a)). We recall that this threshold separates the spectrum into two regions: phase noise above the β-separation line will have a strong impact on the width of the comb teeth and its stability, whereas phase noise under this line will mainly contribute to the wings of the spectrum without any significant impact on stability [42]–[44]. This means that the phase noise added by the FSR division process is too weak to affect the stability of the comb or the linewidth of its teeth. Such a low noise performance is observed for all tested values of m (up to 1000), as shown in Fig. 3(b), which summarizes the results on the measured integrated phase noise for the different evaluated FSR division factors.

3.3 Spectral Shape and Bandwidth

Another key feature of SSI-based FSR control is that the generated ultra-dense OFCs preserve the original spectral shape (including bandwidth) of the input comb. For example, all the output OFCs reported here feature a broad bandwidth of ~10 THz measured at 5 dB from the spectrum peak. This implies that for the case of $m = 1000$, the generated comb comprises more than 40 000 000 spectral lines within this 5-dB bandwidth. Fig. 6 shows the measured full-width spectra of some of the generated ultra-dense OFCs. The initial OFC spectrum is also shown for reference. The two inset figures zoom into two regions spaced at 9 THz (70 nm), for the case $m = 2$, to show the individual spectral lines. The generated comb envelopes remain unchanged for all values of m, whereas the FSR of the resulting comb is divided by the factor m, as induced by the SSI effect.

4. Discussions

The increase of the phase noise with m is attributed to imperfections in the temporal phase modulation signal. Achieving higher FSR division factors requires modulation signals with an increased resolution in the voltage level as the number of modulation phase levels scales up with m. However, this resolution is kept constant in our experiments as it is defined by the AWG's bandwidth and bit depth. Therefore, the experimental modulation signal deviates more strongly from the ideal one
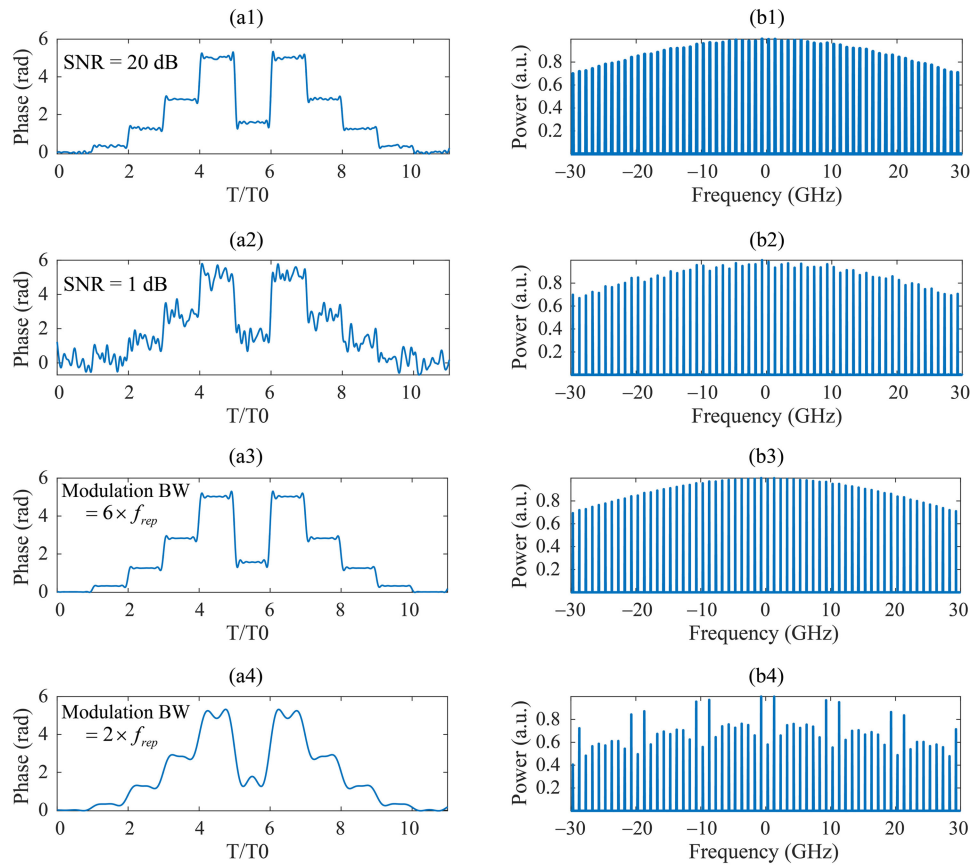
Fig. 5. (a1–a4) The temporal phase modulation signals used to divide the input OFC's FSR by $m = 10$. a1 and a2 have an SNR of 20 dB and 1 dB, respectively, and a modulation bandwidth BW $= 8 \times f_{rep}$. a3 and a4 have a high SNR of 40 dB and a modulation bandwidth of $6 \times f_{rep}$ and $2 \times f_{rep}$, respectively. (b1–b4) Optical spectra of the corresponding output OFCs.

as the FSR division factor m is increased. This effect could be mitigated by using an AWG with a broader bandwidth and/or a larger bit depth. Nevertheless, the low phase noise levels measured in our experiment, including for $m = 1000$, show that the practical modulation imperfections have a very weak effect on the phase noise of the generated OFC: for instance, the integrated phase noise increased less than 8-fold when the division factor m increased 500-fold, from 2 to 1000.

These experimental results agree well with our numerical simulations summarized in Fig. 5, which show that practical modulation imperfections (intensity noise in the modulation signal and limited modulation bandwidth) introduce line-to-line intensity (i.e., envelope) fluctuations in the generated OFCs, but without affecting the FSR and the CEO frequency of the output comb. To perform these simulations, we assumed an OFC formed by a periodic train of 1000 Gaussian pulses with a time-domain repetition period T0 = 0.1 ns, corresponding to an FSR $f_{rep} = 10$ GHz, a carrier frequency $f_c = 300 \times f_{rep}$, and a carrier-envelope-offset $f_{CEO} = f_{rep} \times 3/100$. We used a total number of samples of 10^5, which gives a frequency resolution of $f_{rep}/1000$.

The temporal modulation waveform is expected to exhibit both intensity noise and a limited frequency bandwidth; this is mainly imposed by the equipment employed for waveform generation, such as the electronic AWG used in our experiments. To model these two effects, we used a numerical low pass filter to limit the bandwidth of the modulation signal, and subsequently, we added white intensity noise on top of the filtered modulation. We set the modulation signal bandwidth to $8 \times f_{rep}$ and simulated the output combs obtained for $m = 10$ with signal-to-noise ratios (SNRs) equal to 20 dB and 1 dB, respectively. The resulting output OFCs are shown on Fig. 5 (b1, b2) respectively, and the corresponding modulation signals on Fig. 5(a1, a2). These results show that

the expected FSR division process is successfully achieved in all cases; additionally, it is also observed that the CEO frequency value, f_{CEO}, remains unchanged irrespective of the SNR of the temporal phase modulation profile.

Afterward, we repeated the simulations by setting the SNR = 40 dB and varying the modulation bandwidth to $6 \times f_{rep}$ and $2 \times f_{rep}$. The modulation signals and corresponding output OFCs are shown in Fig. 5 (a3-a4) and (b3-b4), respectively. The obtained OFCs exhibit again the expected divided FSR, with no observable variation in the CEO frequency value. Nonetheless, these results show that the output frequency comb is more sensitive to the modulation bandwidth limitation: a constraint in the modulation bandwidth of $2 \times f_{rep}$ induces about 40% line-to-line intensity fluctuations in the output OFC.

Both the intensity noise and the limited bandwidth induce fluctuations in the phase level of the modulation signal as compared to the ideal case. The different behaviors on the output OFCs can be explained by the intrinsic noise-mitigation capabilities of the SSI effect [35], [37], [45]–[47]. Recall that in SSI, all the input pulses spaced by m/f_{rep} are ideally modified by the same phase modulation level as determined by Eq. (1). Thus, in the case of intensity noise, the impact of random fluctuations of this level is ultimately averaged out across all these pulses. In contrast, the limitation in the modulation bandwidth translates into periodic and deterministic fluctuations in the applied phase levels, which cannot be mitigated by the SSI effect itself. Owing to this periodicity, the fluctuations change the structure of the output OFC by causing strong line-to-line fluctuations along its frequency spectrum, as shown in Fig. 5 (b4). However, similarly to the case of added white noise, in all the conducted simulations, the CEO frequency value remained unchanged, regardless of the modulation bandwidth. This demonstrates further the robustness of the proposed method, in regards to CEO stabilization and the induced FSR division process, against practical imperfections in the temporal modulation signal.

5. Conclusion

We have shown that spectral self-imaging allows for the generation of low noise, CEO-stabilized, and broadband ultra-dense OFCs with programmable FSR, spanning 3 orders of magnitude, from 250 MHz to 250 kHz, in the reported experiments. The presented method is robust against modulation imperfections and preserves the energy, the bandwidth, and the CEO-stabilization of the input comb. The required process, just involving a suitable temporal phase modulation stage, is very simple and independent of the specifications (e.g., cavity dimensions) of the original OFC laser technology. Furthermore, the modulation speed is determined only by the input FSR and does not increase with the division factor, a highly convenient feat given the wide availability of MHz-range electronic equipment. As such, SSI is readily accessible for application on any available OFC generation platform, for example, conventional CEO-stabilized mode-locked lasers (such as in the demonstration shown here) or integrated semiconductor OFCs [48], [49], offering the possibility of adapting the comb's FSR to far below the present capabilities of these technologies. This would enable for comb generation to fulfill the specifications of a host of demanding applications in different fields, including real-time spectroscopy with very high resolution and frequency accuracy.

Appendix

A. CEO-Frequency Stability of the Input OFC

The input OFC is generated from a commercial mode-locked fiber laser (Menlo-UL250), with a stabilized CEO frequency of $f_{CEO} = 20$ MHz. To showcase the CEO stability performance of the input OFC, the evolution of f_{CEO} in time and its Allan deviation is shown in Fig. 6.

B. Equations for Heterodyne Detection of Two OFCs

To obtain the spectrum's expression of the heterodyne product of two OFCs, we consider the general case of two combs with different repetition rates, $f_{rep}^{(1)}$ and $f_{rep}^{(2)}$. The optical frequencies $\nu_M^{(1)}$
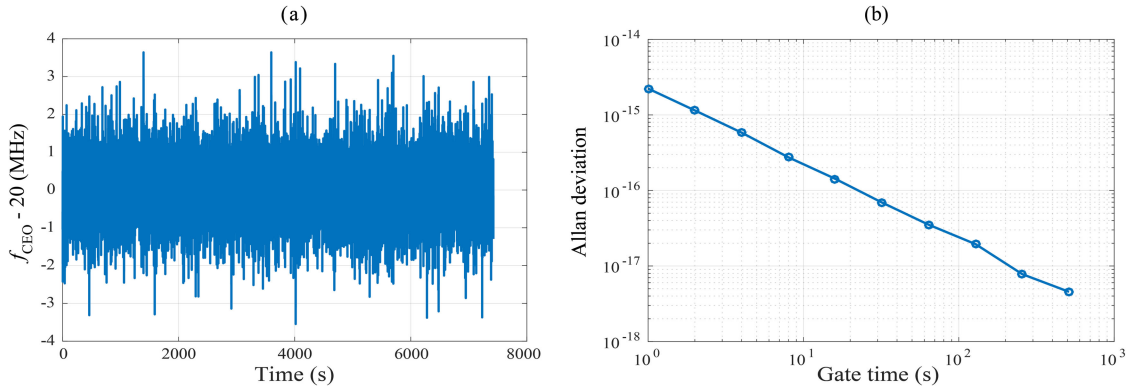
Fig. 6. (a) Evolution of the input OFC offset frequency $-f_{CEO}-$ as a function of time. (b) Allan deviation for f_{CEO}.

and $\nu_N^{(2)}$ correspond to the Mth line of Comb 1 and the Nth line of Comb 2, respectively, and they can be expressed as:

$$\nu_M^{(1)} = Mf_{rep}^{(1)} + f_{CEO}^{(1)} + \Delta f_{rep}^{(1)}(t) + \Delta f_{CEO}^{(1)}(t)$$

$$\nu_N^{(2)} = Nf_{rep}^{(2)} + f_{CEO}^{(2)} + \Delta f'_{rep}(t) + \Delta f'_{CEO}(t) \tag{A1}$$

where $\Delta f_{rep}(t)$ and $\Delta f_{CEO}(t)$ represent the repetition rate noise and the f_{CEO} noise, respectively. They are modelled as Gaussian noise sources ($\mathcal{N}(\mu, \sigma^2)$) that satisfy the usual zero-mean and delta-correlated properties:

$$\Delta f_{rep}^{(i)}(t) \sim \mathcal{N}\left(0, \sigma_{rep}^2(i)\right)$$

$$\Delta f_{CEO}^{(i)}(t) \sim \mathcal{N}\left(0, \sigma_{CEO}^2(i)\right)$$

$$\langle \Delta f_{rep}^{(i)}(t)\ \Delta f_{rep}^{(i)}(t')\rangle = \delta\left(t - t'\right)$$

$$\langle \Delta f_{CEO}^{(i)}(t)\ \Delta f_{CEO}^{(i)}(t')\rangle = \delta\left(t - t'\right) \tag{A2}$$

where $\sigma_{rep}^2(i)$, $\sigma_{CEO}^2(i)$ are the variances of the Gaussian noise sources $\Delta f_{rep}^{(i)}(t)$ and $\Delta f_{CEO}^{(i)}(t)$, respectively. In our case, Comb 2 (output) is obtained by transforming Comb 1 (input), so we can write:

$$f_{rep}^{(2)} = \frac{1}{m}\ f_{rep}^{(1)} \tag{A3}$$

Therefore, the noise sources in $\nu_N^{(2)}$ can be split into two parts: (i) Noise sources (of the FSR and the CEO, i.e., f_{rep} and f_{CEO}) that are initially present in Comb 1 and transferred to Comb 2, which are referred to as $\Delta f_{rep}^{(2)}(t)$ and $\Delta f_{CEO}^{(2)}(t)$, respectively. When the two arms of the heterodyne setup are shorter than the OFC's coherence length, as in our experiments, these sources correlate strongly with their counterparts in $\nu_N^{(1)}$. (ii) Noise sources that are present in $\nu_N^{(2)}$ and do not correlate with any of the noise in $\nu_N^{(1)}$. They represent a possible excess noise added during the FSR division process. We refer to them as $\Delta f_{rep}^{excess}(t)$ and $\Delta f_{CEO}^{excess}(t)$. According to these definitions, $\Delta f'_{rep}(t)$ and $\Delta f'_{CEO}(t)$ in Eq. A1 can be written as the sum of these correlated and uncorrelated noise sources

$$\Delta f'_{rep}\ (t) = \Delta f_{rep}^{(2)}(t) +\ \Delta f_{rep}^{excess}(t)$$

$$\Delta f'_{CEO}\ (t) = \Delta f_{CEO}^{(2)}(t) + \Delta f_{CEO}^{excess}(t) \tag{A4}$$

Let us also assume that

$$f_{CEO}^{(2)} = f_{CEO}^{(1)} + \delta f_{CEO} \tag{A5}$$

where δf_{CEO} represents a possible drift of the original f_{CEO} during the FSR division process. The beat signal between $\nu_N^{(2)}$ and $\nu_M^{(1)}$ now reads

$$\nu_N^{(2)} - \nu_M^{(1)} = f_{rep}^{(1)}[N/m - M] + \overbrace{\left(\Delta f_{rep}^{(2)}(t) - \Delta f_{rep}^{(1)}(t)\right)}^{=\Delta f_{rep}^{(21)}(t)} + \overbrace{\left(\Delta f_{CEO}^{(2)}(t) - \Delta f_{CEO}^{(1)}(t)\right)}^{=\Delta f_{CEO}^{(21)}(t)} + \cdots$$
$$\delta f_{CEO} + \Delta f_{rep}^{excess}(t) + \Delta f_{CEO}^{excess}(t) \tag{A6}$$

All the noise terms in Eq. A6 possess a normal distribution characterized by their respective variances. Let us focus on $\Delta f_{rep}^{(21)}(t)$ and $\Delta f_{CEO}^{(21)}(t)$, characterized by their variances σ_r^2 and σ_c^2 as follows

$$\Delta f_{rep}^{(21)}(t) \sim \mathcal{N}\left(\sigma_r^2\right); \quad \sigma_r^2 = \sigma_{rep}^2(2) + \sigma_{rep}^2(1) - 2\sigma_{rep}(2,1)$$
$$\Delta f_{CEO}^{(21)}(t) \sim \mathcal{N}\left(\sigma_c^2\right); \quad \sigma_c^2 = \sigma_{CEO}^2(2) + \sigma_{CEO}^2(1) - 2\sigma_{CEO}(2,1) \tag{A7}$$

where $\sigma(p,q)$ is the covariance term. Eq. A7 implies that the noise sources initially present in the input OFC (i.e., $\Delta f_{rep,CEO}^{(1)}(t)$ and $\Delta f_{rep,CEO}^{(2)}(t)$) cancel out in the heterodyne product. This can be demonstrated by writing the covariance in terms of the correlation $\sigma(p,q) = \rho(p,q)\sigma(p)\sigma(q)$. For example, when $\Delta f_{rep}^{(1)}(t)$ correlates with $\Delta f_{rep}^{(2)}(t)$, $\sigma_{rep}^2(1) = \sigma_{rep}^2(2)$ and $\rho(2,1) = 1$, which leads to $\sigma_r^2 = 0$. As a result, both $\Delta f_{rep}^{(21)}(t)$ and $\Delta f_{CEO}^{(21)}(t)$ vanish and only the potential excess noise that may result from the FSR division process remains. Hence, the heterodyne product can be written as follows

$$\nu_N^{(2)} - \nu_M^{(1)} = f_{rep}^{(1)}(N/m - M) + \delta f_{CEO} + \Delta f_{rep}^{excess}(t) + \Delta f_{CEO}^{excess}(t) \tag{A8}$$

This equation is identical to Eq. (2) in the main text.

References

[1] S. A. Diddams, "The evolving optical frequency comb," *J. Opt. Soc. Amer. B*, vol. 27, no. 11, pp. B51–B62, 2010.
[2] H. R. Telle, G. Steinmeyer, A. E. Dunlop, J. Stenger, D. H. Sutter, and U. Keller, "Carrier-envelope offset phase control: A novel concept for absolute optical frequency measurement and ultrashort pulse generation," *Appl. Phys. B Lasers Opt.*, vol. 69, no. 4, pp. 327–332, 1999.
[3] T. Udem, R. Holzwarth, and T. W. Hänsch, "Optical frequency metrology," *Nature*, vol. 416, no. 6877, pp. 233–237, 2002.
[4] J. Ye, H. Schnatz, and L. W. Hollberg, "Optical frequency combs: From frequency metrology to optical phase control," *IEEE J. Sel. Topics Quantum Electron.*, vol. 9, no. 4, pp. 1041–1058, Jul./Aug. 2003.
[5] R. Van Rooij *et al.*, "Frequency metrology in quantum degenerate helium: Direct measurement of the 2 3S1→2 1S0 transition," *Science*, vol. 333, no. 6039, pp. 196–198, 2011.
[6] B. Lomsadze and S. T. Cundiff, "Frequency combs enable rapid and high-resolution multidimensional coherent spectroscopy," *Science*, vol. 357, no. 6358, pp. 1389–1391, 2017.
[7] Y. Bao *et al.*, "A digitally generated ultrafine optical frequency comb for spectral measurements with 0.01-pm resolution and 0.7-μs response time," *Light Sci. Appl.*, vol. 4, no. 6, 2015, Art. no. e300.
[8] S. Bartalini *et al.*, "Frequency-comb-assisted terahertz quantum cascade laser spectroscopy," *Phys. Rev. X*, vol. 4, no. 2, 2014, Art. no. 021006.
[9] H. Fattahi *et al.*, "Third-generation femtosecond technology," *Optica*, vol. 1, no. 1, pp. 45–63, 2014.
[10] F. Krausz, "The birth of attosecond physics and its coming of age," *Physica Scripta*, vol. 91, no. 6, 2016, Art. no. 063011.
[11] S. Droste, G. Ycas, B. R. Washburn, I. Coddington, and N. R. Newbury, "Optical frequency comb generation based on Erbium fiber lasers," *Nanophotonics*, vol. 5, no. 2, pp. 196–213, 2016.
[12] J. Kim and Y. Song, "Ultralow-noise mode-locked fiber lasers and frequency combs: principles, status, and applications," *Adv. Opt. Photon.*, vol. 8, no. 3, pp. 465–540, Sep. 2016.
[13] T. Ideguchi, A. Poisson, G. Guelachvili, N. Picqué, and T. W. Hänsch, "Adaptive real-time dual-comb spectroscopy," *Nature Commun.*, vol. 5, 2014, Art. no. 3375.
[14] G. Millot *et al.*, "Frequency-agile dual-comb spectroscopy," *Nature Photon.*, vol. 10, pp. 27–30, Dec. 2015.
[15] I. Coddington, N. Newbury, and W. Swann, "Dual-comb spectroscopy," *Optica*, vol. 3, no. 4, pp. 414–426, Apr. 2016.

[16] D. A. Long, A. J. Fleisher, D. F. Plusquellic, and J. T. Hodges, "Electromagnetically induced transparency in vacuum and buffer gas potassium cells probed via electro-optic frequency combs," *Opt. Lett.*, vol. 42, no. 21, pp. 4430–4433, 2017.

[17] D. A. Long, A. J. Fleisher, D. F. Plusquellic, and J. T. Hodges, "Multiplexed sub-Doppler spectroscopy with an optical frequency comb," *Phys. Rev. A*, vol. 94, no. 6, 2016, Art. no. 061801.

[18] M. Kleinert, M. G. Dahl, and S. Bergeson, "Measurement of the Yb I S 0 1−P 1 1 transition frequency at 399 nm using an optical frequency comb," *Phys. Rev. A*, vol. 94, no. 5, 2016, Art. no. 052511.

[19] J. Liu *et al.*, "Dispersion characterization of microresonators for broadband Kerr frequency comb generation," in *Proc. Conf. Lasers Electro-Opt.*, 2017, pp. 1–2.

[20] P. Del'Haye, O. Arcizet, M. L. Gorodetsky, R. Holzwarth, and T. J. Kippenberg, "Frequency comb assisted diode laser spectroscopy for measurement of microcavity dispersion," *Nature Photon.*, vol. 3, no. 9, pp. 529–533, 2009.

[21] G. B. Rieker *et al.*, "Frequency-comb-based remote sensing of greenhouse gases over kilometer air paths," *Optica*, vol. 1, no. 5, pp. 290–298, 2014.

[22] A. Parriaux, K. Hammani, and G. Millot, "Two-micron all-fibered dual-comb spectrometer based on electro-optic modulators and wavelength conversion," *Commun. Phys.*, vol. 1, no. 1, May 2018, Art. no. 17.

[23] S. Mahadevan and J. Ge, "The use of absorption cells as a wavelength reference for precision radial velocity measurements in the near-infrared," *Astrophysical J.*, vol. 692, no. 2, 2009, Art. no. 1590.

[24] F. S. Vieira, F. C. Cruz, D. F. Plusquellic, and S. A. Diddams, "Tunable resolution terahertz dual frequency comb spectrometer," *Opt. Exp.*, vol. 24, no. 26, pp. 30100–30107, 2016.

[25] T. Yasui *et al.*, "Super-resolution discrete Fourier transform spectroscopy beyond time-window size limitation using precisely periodic pulsed radiation," *Optica*, vol. 2, no. 5, pp. 460–467, 2015.

[26] F. Riehle, "Towards a redefinition of the second based on optical atomic clocks," *Comptes Rendus Physique*, vol. 16, no. 5, pp. 506–515, 2015.

[27] R. Le Targat *et al.*, "Experimental realization of an optical second with strontium lattice clocks," *Nature Commun.*, vol. 4, 2013, Art. no. 2109.

[28] N. B. Hébert, V. Michaud-Belleau, S. Magnan-Saucier, J.-D. Deschênes, and J. Genest, "Dual-comb spectroscopy with a phase-modulated probe comb for sub-MHz spectral sampling," *Opt. Lett.*, vol. 41, no. 10, pp. 2282–2285, 2016.

[29] V. Torres-Company and A. M. Weiner, "Optical frequency comb technology for ultra-broadband radio-frequency photonics," *Laser Photon. Rev.*, vol. 8, no. 3, pp. 368–393, 2014.

[30] H. G. de Chatellus, L. R. Cortés, and J. Azaña, "Arbitrary energy-preserving control of the line spacing of an optical frequency comb over six orders of magnitude through self-imaging," *Opt. Exp.*, vol. 26, no. 16, pp. 21069–21085, 2018.

[31] A. Malacarne and J. Azaña, "Discretely tunable comb spacing of a frequency comb by multilevel phase modulation of a periodic pulse train," *Opt. Exp.*, vol. 21, no. 4, pp. 4139–4144, 2013.

[32] J. Caraquitena, M. Beltrán, R. Llorente, J. Martí, and M. A. Muriel, "Spectral self-imaging effect by time-domain multilevel phase modulation of a periodic pulse train," *Opt. Lett.*, vol. 36, no. 6, pp. 858–860, 2011.

[33] R. Maram and J. Azaña, "Spectral self-imaging of time-periodic coherent frequency combs by parabolic cross-phase modulation," *Opt. Exp.*, vol. 21, no. 23, Nov. 2013, Art. no. 28824.

[34] M. Seghilani, R. Maram, L. R. Cortes, and J. Azana, "Generation of a 128-GHz optical pulse train from a 250-MHz frequency comb using temporal self-imaging," *presented at the IEEE Photon. Conf.*, Orlando, FL, USA, 2017, pp. 141–142.

[35] X. Z. Li and J. Azaña, "On mode-spacing division of a frequency comb by temporal phase modulation," *IEEE J. Sel. Topics Quantum Electron.*, vol. 25, no. 4, pp. 1–10, Jul./Aug. 2018.

[36] Q. Xie, B. Zheng, and C. Shu, "Adjustable repetition-rate multiplication of optical pulses using fractional temporal Talbot effect with preceded binary intensity modulation," *Opt. Commun.*, vol. 391, pp. 16–23, 2017.

[37] R. Maram *et al.*, "Demonstration of input-to-output gain and temporal noise mitigation in a Talbot amplifier," *IEEE Photon. Technol. Lett.*, vol. 30, no. 8, pp. 665–668, Apr. 2018.

[38] S. T. Cundiff, "Phase stabilization of ultrashort optical pulses," *J. Phys. Appl. Phys.*, vol. 35, no. 8, 2002, Art. no. R43.

[39] I. Coddington, W. C. Swann, and N. R. Newbury, "Coherent multiheterodyne spectroscopy using stabilized optical frequency combs," *Phys. Rev. Lett.*, vol. 100, no. 1, 2008, Art. no. 013902.

[40] J. Davila-Rodriguez, C. Williams, M. Akbulut, and P. J. Delfyett, "Multi-heterodyne characterization of multi-gigahertz spaced optical frequency comb sources," in *Proc. Lasers Electro-Opt., Quantum Electron. Laser Sci. Conf.*, 2010, pp. 1–2.

[41] N. Von Bandel, M. Myara, M. Sellahi, T. Souici, R. Dardaillon, and P. Signoret, "Time-dependent laser linewidth: Beat-note digital acquisition and numerical analysis," *Opt. Exp.*, vol. 24, no. 24, pp. 27961–27978, 2016.

[42] G. Di Domenico, S. Schilt, and P. Thomann, "Simple approach to the relation between laser frequency noise and laser line shape," *Appl. Opt.*, vol. 49, no. 25, Sep. 2010, Art. no. 4801.

[43] E. S. Lamb, D. R. Carlson, D. D. Hickstein, J. R. Stone, S. A. Diddams, and S. B. Papp, "Optical-frequency measurements with a Kerr microcomb and photonic-chip supercontinuum," *Phys. Rev. Appl.*, vol. 9, no. 2, Feb. 2018, Art. no. 024030.

[44] T. Puppe, A. Sell, R. Kliese, N. Hoghooghi, A. Zach, and W. Kaenders, "Characterization of a DFG comb showing quadratic scaling of the phase noise with frequency," *Opt. Lett.*, vol. 41, no. 8, Apr. 2016, Art. no. 1877.

[45] R. Maram, J. Van Howe, M. Li, and J. Azaña, "Noiseless intensity amplification of repetitive signals by coherent addition using the temporal Talbot effect," *Nature Commun.*, vol. 5, Oct. 2014, Art. no. 5163.

[46] C. R. Fernández-Pousa *et al.*, "Timing jitter smoothing by Talbot effect. I. Variance," *J. Opt. Soc. Amer. B*, vol. 21, no. 6, pp. 1170–1177, 2004.

[47] L. Romero Cortés, R. Maram, and J. Azaña, "Fractional averaging of repetitive waveforms induced by self-imaging effects," *Phys. Rev. A*, vol. 92, no. 4, Oct. 2015, Art. no. 041804.

[48] Z. Wang *et al.*, "A III–V-on-Si ultra-dense comb laser," *Light Sci. Appl.*, vol. 6, no. 5, 2017, Art. no. e16260.

[49] V. Corral, R. Guzmán, C. Gordón, X. Leijtens, and G. Carpintero, "Optical frequency comb generator based on a monolithically integrated passive mode-locked ring laser with a Mach–Zehnder interferometer," *Opt. Lett.*, vol. 41, no. 9, pp. 1937–1940, 2016.